


# Mechanical Control of Nonlinearity in Doubly Clamped MEMS Beam Resonators Using Preloaded Lattice-Mismatch Strain

Chao Li<sup>1,†</sup>, Boqi Qiu<sup>2,‡</sup>, Yuri Yoshioka,<sup>1</sup> Kazuhiko Hirakawa,<sup>2,3,\*</sup> and Ya Zhang<sup>1,†</sup>

<sup>1</sup>*Institute of Engineering, Tokyo University of Agriculture and Technology, Koganei-shi, Tokyo, 184-8588, Japan*

<sup>2</sup>*Institute of Industrial Science, University of Tokyo, 4-6-1 Komaba, Meguro-ku, Tokyo 153-8505, Japan*

<sup>3</sup>*Institute for Nano Quantum Information Electronics, University of Tokyo, 4-6-1 Komaba, Meguro-ku, Tokyo 153-8505, Japan*

 (Received 26 April 2022; revised 19 October 2022; accepted 23 December 2022; published 9 February 2023)

We theoretically clarify the mechanism of the strain-tuning effect for control of the mechanical nonlinearity in doubly clamped MEMS beam resonators and experimentally demonstrate that nonlinearity can be effectively suppressed with a preloaded lattice-mismatch strain in the MEMS beam. Mechanical nonlinearity arises from the hardening- and softening-nonlinearity terms in the Duffing motion equation of the MEMS beam. By approaching the buckling condition of the MEMS beam, the substantially increased softening nonlinearity greatly compensates for the hardening nonlinearity, resulting in suppression of the total nonlinearity. Utilizing this knowledge, we fabricate  $\text{In}_x\text{Ga}_{1-x}\text{As}$  MEMS beams with a preloaded lattice-mismatch strain, which is achieved by adding a small amount ( $x = \sim 0.4\%$ ) of indium to the GaAs MEMS beam during wafer growth. The buckling condition in the experiment is achieved by carefully modulating the length of the  $\text{In}_x\text{Ga}_{1-x}\text{As}$  MEMS beams. As a result, mechanical nonlinearity is largely modulated from hardening to softening and reaches a quasiszero value near the buckling condition, demonstrating the effectiveness of using lattice mismatch for controlling the mechanical nonlinearity of MEMS resonators.

DOI: [10.1103/PhysRevApplied.19.024025](https://doi.org/10.1103/PhysRevApplied.19.024025)

## I. INTRODUCTION

Microelectromechanical system (MEMS) resonators [1–3] are promising candidates for high-sensitivity sensing applications. MEMS resonators can detect small shifts in the resonance frequency owing to the high-quality ( $Q$ ) factors. This property is utilized for the detection of mass [4–6], spin orientation [7], charge [8–10], temperature [11,12], and infrared radiation [13,14]. Previously, we reported using a doubly clamped MEMS beam resonator as a fast and sensitive bolometer for terahertz (THz) detection [15,16]. The MEMS beam is heated up owing to the absorption of THz electromagnetic waves, and the induced thermal strain shifts the resonance frequency of the MEMS resonator. In sensing applications with MEMS resonators, a large linear oscillation amplitude is generally preferable to reduce the frequency noise and improve the signal-to-noise ratio [17], which can be achieved by increasing the driving force. However, with increasing oscillation amplitude, the MEMS resonators commonly enter the nonlinear-oscillation region because of mechanical nonlinearity, where hysteretic oscillations and increased frequency noise

are observed [18,19]. The control of mechanical nonlinearity is therefore desirable for achieving the low-noise operation of MEMS resonators.

Recently, we reported on controlling the mechanical nonlinearity of MEMS beam resonators through a thermal strain-tuning effect [20]. We observe a significant reduction in the mechanical nonlinearity near the buckling point of the MEMS beam. However, the origin of such thermal strain tuning on mechanical nonlinearity has not yet been theoretically clarified. Moreover, controlling the nonlinearity by the thermal effect requires additional heating of the MEMS beam, which increases the noise and frequency drift coming from the thermal effect. Thermal strain is not the only method to buckle the MEMS beam. It is reported that the buckling condition of the MEMS beam can be precisely controlled by preloading a lattice-mismatch strain [21], which can be achieved during the wafer-growth stage without the requirement for additional heating. Therefore, the use of a lattice mismatch would be a promising approach to control the mechanical nonlinearity of the MEMS beam resonators.

Here, we clarify the mechanism of the strain-tuning effect on the control of mechanical nonlinearity in doubly clamped MEMS beam resonators, and then demonstrate that nonlinearity can be effectively suppressed with a preloaded lattice-mismatch strain in the MEMS beam.

\*hirakawa@iis.u-tokyo.ac.jp

†zhangya@go.tuat.ac.jp

‡Chao Li and Boqi Qiu contributed equally to this work.

The nonlinearity of the MEMS beam arises from the cubic (hardening) and quadratic (softening) nonlinearity terms in the Duffing motion equation. With strain tuning, nonlinearity can be well suppressed when approaching the buckling condition of the MEMS beam. This is because the steep increase in softening nonlinearity near the buckling condition greatly compensates for hardening nonlinearity, resulting in the suppression of total nonlinearity. Utilizing this knowledge, we fabricate  $\text{In}_x\text{Ga}_{1-x}\text{As}$  MEMS beams with a preloaded lattice-mismatch strain, which is achieved by adding a small amount ( $x \sim 0.4\%$ ) of indium to the GaAs MEMS beam during wafer growth. The buckling condition in the experiment is achieved by carefully modulating the length of the  $\text{In}_x\text{Ga}_{1-x}\text{As}$  MEMS beams. We estimate the total nonlinearity in the MEMS beam by measuring its resonance-frequency shift as a function of oscillation amplitude. As a result, nonlinearity is largely modulated from hardening to softening as  $L$  increases and reaches a quasizero value near the buckling condition, demonstrating the effectiveness of using lattice mismatch for controlling the mechanical nonlinearity of MEMS resonators. Furthermore, we introduce the effective nonlinearity,  $Y_{(\alpha,\beta)}$ , to reproduce the total nonlinearity in the MEMS beam, which intuitively shows the effect of hardening and softening nonlinearities on the total nonlinearity, allowing one to understand the origin of the nonlinearity change.

## II. EQUATION OF MOTION

The Duffing equation, with quadratic and cubic nonlinearities, is commonly utilized for studying the nonlinear-resonance behavior of MEMS resonators [22–26]. For an initially straight doubly clamped MEMS beam resonator with length  $L$ , the motion equation of its transverse vibrations is approximately described by the Euler-Bernoulli equation as [23]

$$\rho S \frac{\partial^2 X}{\partial t^2} = -EI \frac{\partial^4 X}{\partial u^4} + T \frac{\partial^2 X}{\partial u^2} \quad (1)$$

with the following boundary conditions:

$$X|_{u=0,L} = 0 \text{ and } \left. \frac{\partial X}{\partial u} \right|_{u=0,L} = 0, \quad (2)$$

where  $X(u,t)$  is the transverse displacement from equilibrium;  $u$  is the coordinate along the length of the beam;  $t$  is the timescale;  $\rho$  is the density;  $E$  is the Young's modulus;  $L$  is the beam length;  $S$  and  $I$  denote the cross-section area and the moment of inertia, respectively ( $S = bh$  and  $I = bh^3/12$  for beams with rectangular cross sections, with  $b$  and  $h$  being the width and thickness of the MEMS beam, respectively);  $T$  is the tension in the MEMS beam, which is composed of its inherent tension,  $T_0$  (positive for a tensile force and negative for a compressive force), and the

additional tension,  $\Delta T$ , coming from extension of the beam length ( $\Delta L$ ) in the vibration.

Here, we consider only the first bending mode of the MEMS beam, where mechanical nonlinearity is affected by internal strain the most. We assume that the transverse displacement of the MEMS beam can be expressed as the product of the mode profile function,  $\phi(u)$ , and the central displacement of the beam,  $x(t)$ , as

$$X(u,t) = \phi(u)x(t). \quad (3)$$

Then, we can obtain a Duffing equation of motion for the MEMS beam [23]:

$$\ddot{x} + \left[ \frac{EI}{\rho S} \frac{\int (\phi^{uu})^2 du}{\int \phi^2 du} + \frac{T_0}{\rho S} \frac{\int (\phi^u)^2 du}{\int \phi^2 du} \right] x + \left[ \frac{E}{2\rho L} \frac{(\int (\phi^u)^2 du)^2}{\int \phi^2 du} \right] x^3 = 0, \quad (4)$$

where  $\phi^u = \partial\phi/\partial u$  and  $\phi^{uu} = \partial^2\phi/\partial u^2$ . As seen in Eq. (4), the cubic nonlinearity coefficient is  $\alpha = (E/2\rho L) \left( (\int (\phi^u)^2 du)^2 / \int \phi^2 du \right) > 0$ , which gives a hardening nonlinearity [22,27].

Next, we consider a MEMS beam with an initial center deflection of  $x_0$ . When a compressive strain,  $\varepsilon$ , is introduced into the beam, the center deflection increases to  $x_T$ , as schematically shown in Fig. 1(a). The steady-state equation under this condition is expressed as

$$EI(x_T - x_0) \int (\phi^{uu})^2 du + T_0 x_T \int (\phi^u)^2 du = 0, \quad (5)$$

from which we can derive  $x_T$  as a function of the initial center deflection,  $x_0$ , and inherent tension,  $T_0$ :

$$x_T = \frac{EI \int (\phi^{uu})^2 du}{EI \int (\phi^{uu})^2 du + T_0 \int (\phi^u)^2 du} x_0. \quad (6)$$

Here, the inherent tension,  $T_0 = ES\varepsilon_r$ , is different from the induced compressive load,  $T = ES\varepsilon$ , since part of the compressive strain,  $\varepsilon$ , is released by the increased center deflection. The residual strain,  $\varepsilon_r$ , is expressed as

$$\varepsilon_r = \varepsilon - \frac{(x_T^2 - x_0^2)}{2L} \int (\phi^u)^2 du. \quad (7)$$

The beam length extends when it differs from its equilibrium position in the oscillation with an additional displacement,  $x$ , as

$$\begin{aligned} \Delta L &= \frac{(x + x_T)^2 - x_T^2}{2} \int_0^L du \left( \frac{\partial\phi}{\partial u} \right)^2 \\ &= \frac{x^2 + 2x_T x}{2} \int_0^L du \left( \frac{\partial\phi}{\partial u} \right)^2, \end{aligned} \quad (8)$$

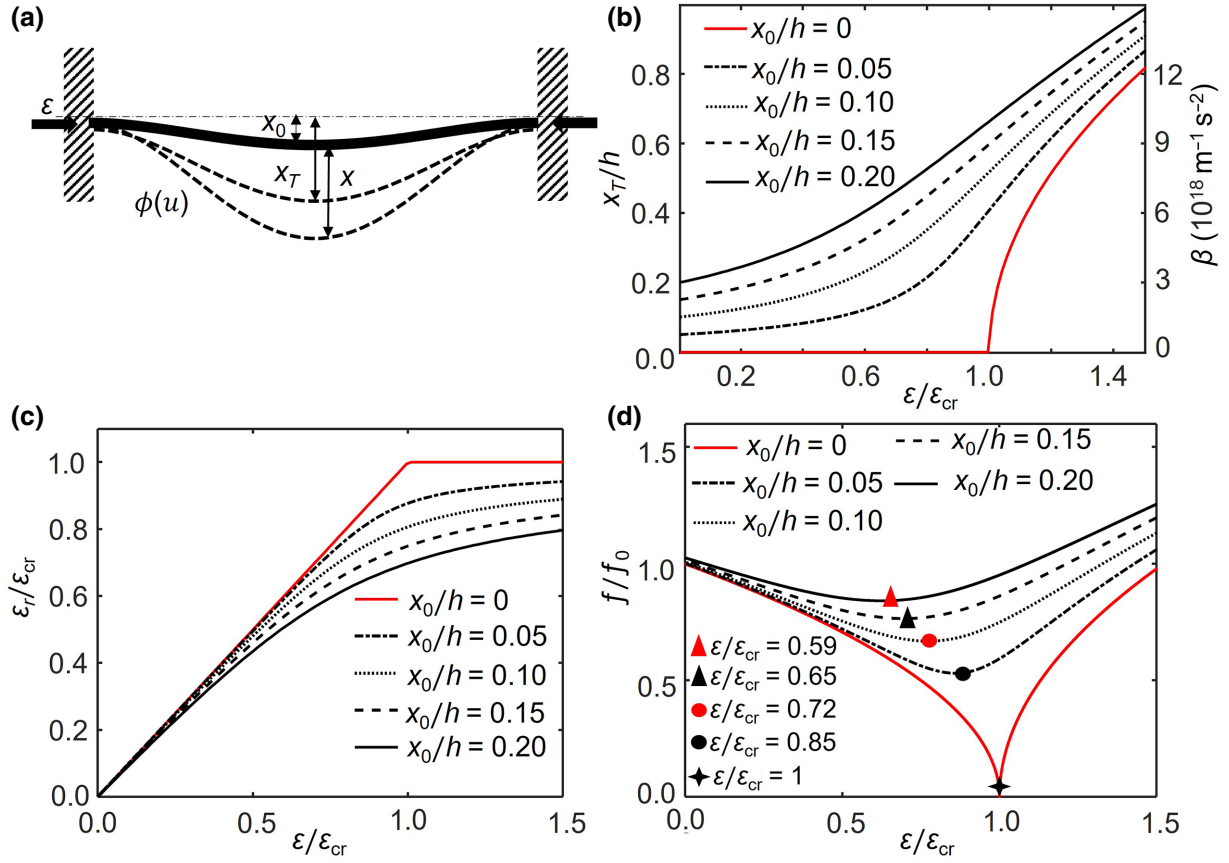


FIG. 1. (a) Schematic diagram of a MEMS beam with an initial center deflection in the steady state and oscillatory state. When the center deflection increases from  $x_0$  to  $x_T$ , the MEMS beam has a new equilibrium position for the oscillation. (b) Calculated center deflection,  $x_T/h$  (left y axis), and quadratic nonlinearity coefficient,  $\beta$  (right y axis), as a function of compressive strain ( $\epsilon/\epsilon_{cr}$ ) at various initial center deflections ( $x_0/h = 0, 0.05, 0.1, 0.15, 0.2$ ).  $x_0$  and  $x_T$  are normalized by the thickness ( $h$ ) of the MEMS beam, and  $\epsilon$  is normalized by the buckling critical strain,  $\epsilon_{cr}$ , of the MEMS beam. This figure is adapted from Fig. 2(b) of Ref. [20]. (c) Calculated residual strain ( $\epsilon_r/\epsilon_{cr}$ ) as a function of compressive strain ( $\epsilon/\epsilon_{cr}$ ) at various initial center deflections. (d) Calculated resonance frequency ( $f/f_0$ ) as a function of  $\epsilon/\epsilon_{cr}$  at various initial center deflections; frequency is normalized by the natural frequency ( $f_0$ ) without  $\epsilon$ . Buckling points are marked by geometric shapes of different colors. This figure is adapted from Fig. 2(a) of Ref. [20].

$\Delta L$  gives an additional tension,  $\Delta T = ES\Delta L/L$ , to the MEMS beam. With a total tension of  $T = T_0 + \Delta T$ , the motion equation of the MEMS beam becomes

$$\ddot{x} + \left[ \frac{EI}{\rho S} \frac{\int (\phi^{(4)})^2 du}{\int \phi^2 du} + \frac{T_0}{\rho S} \frac{\int (\phi'')^2 du}{\int \phi^2 du} + x_T^2 \frac{E}{\rho L} \frac{\int (\phi'')^2 du}{\int \phi^2 du} \right] x + \left[ \frac{E}{2\rho L} \frac{\int (\phi'')^2 du}{\int \phi^2 du} \right] x^3 + \left[ \frac{3x_T E}{2\rho L} \frac{\int (\phi'')^2 du}{\int \phi^2 du} \right] x^2 = 0. \quad (9)$$

Compared with Eq. (4), by considering an initial center deflection, an additional quadratic nonlinear term,

$\beta = (3x_T E/2\rho L) \left( \frac{\int (\phi'')^2 du}{\int \phi^2 du} \right) = 3x_T \alpha$ , arises. As we discussed in a previous publication [20], the quadratic nonlinear term always gives a softening nonlinearity to the MEMS resonator, which compensates for the cubic hardening nonlinearity and leads to the suppression of total nonlinearity. Furthermore, the quadratic term is proportional to the center deflection,  $x_T$ , indicating that nonlinearity can be suppressed by precisely controlling  $x_T$ .

From Eq. (9), we can see that both the resonance frequency and nonlinearity terms are affected by the mode shape,  $\phi(u)$ . For the first bending mode of a curved MEMS beam,  $\phi(u)$  is usually approximated as [28]

$$\phi(u) = \frac{1}{2} \left( 1 - \cos \frac{2\pi}{L} u \right). \quad (10)$$

By substituting Eq. (10) into Eq. (9), we can express the resonance frequency,  $\omega_0^2$ , and nonlinearity terms as

$$\begin{aligned}\omega_0^2 &= \frac{EI}{\rho S} \frac{16\pi^4}{3L^4} + \frac{T_0}{\rho S} \frac{4\pi^2}{3L^2} + x_T^2 \frac{E}{\rho} \frac{2\pi^4}{3L^4}, \\ \alpha &= \frac{E\pi^4}{3\rho L^4}, \\ \beta &= \frac{E\pi^4}{\rho L^4} x_T = 3x_T \alpha.\end{aligned}\quad (11)$$

By using Eq. (10), Eqs. (6) and (7) can also be simplified as

$$x_T = \frac{1}{1 - (\varepsilon_r/\varepsilon_{cr})} x_0, \quad (12)$$

and

$$\varepsilon_r = \varepsilon - (x_T^2 - x_0^2) \frac{\pi^2}{4L^2}. \quad (13)$$

### III. NUMERICAL ANALYSIS RESULTS

Numerical analysis is performed for the MEMS beam resonators with dimensions of 100 ( $L$ )  $\times$  30 ( $b$ )  $\times$  1  $\mu\text{m}^3$  ( $h$ ) and with  $E = 85.9$  GPa and  $\rho = 5307$  kg/m<sup>3</sup> applied for the Young's modulus and density of the GaAs material, respectively. The left  $y$  axis of Fig. 1(b) plots the normalized center deflection,  $x_T/h$ , as a function of compressive strain,  $\varepsilon/\varepsilon_{cr}$ , calculated for various initial center deflections,  $x_0/h$ . Here,  $\varepsilon_{cr} = (\pi^2/3)(h^2/L^2)$  is Euler's buckling critical strain of the MEMS beam. As seen, in the case of  $x_0 = 0$ , the center deflection,  $x_T$ , remains zero before buckling ( $\varepsilon/\varepsilon_{cr} < 1$ ), and starts to increase with the compressive strain following  $x_T = (2L(\varepsilon - \varepsilon_{cr})/\pi)$  after buckling ( $\varepsilon/\varepsilon_{cr} \geq 1$ ). However, in the case of  $x_0 > 0$ ,  $x_T$  is given by the initial deflection,  $x_0$ , as well as the compressive strain,  $\varepsilon$ , as derived from Eqs. (6) and (7). Under this condition,  $x_T$  increases with  $\varepsilon$ , even when  $\varepsilon < \varepsilon_{cr}$ . This can be understood by the fact that the beam with an initial center deflection tends to bend more when a compressive strain is applied. The residual strain,  $\varepsilon_r$ , in the MEMS beam is plotted as a function of  $\varepsilon/\varepsilon_{cr}$  in Fig. 1(c) with various  $x_T/h$ . When  $x_0 = 0$ ,  $\varepsilon_r$  increases with  $\varepsilon$  in a 1 : 1 ratio until  $\varepsilon = \varepsilon_{cr}$ , and then  $\varepsilon_r$  remains at  $\varepsilon_{cr}$  instead of continuing to increase with  $\varepsilon$ . On the other hand, when  $x_0 > 0$ ,  $\varepsilon_r$  increases with  $\varepsilon$  but never reaches  $\varepsilon_{cr}$ . This is because the increased center deflection from  $x_0$  to  $x_T$  releases part of the compressive strain, thus,  $\varepsilon_r$  is always smaller than  $\varepsilon$  and  $\varepsilon_{cr}$  when  $x_0 > 0$ .

Furthermore, the increased center deflection changes the resonance frequency of the MEMS resonator. Figure 1(d) shows the normalized resonance frequency,  $f/f_0$ , as a function of  $\varepsilon/\varepsilon_{cr}$  calculated for various  $x_0/h$ . When  $x_0/h = 0$ , the frequency drops to zero at  $\varepsilon/\varepsilon_{cr} = 1$  and then increases from zero to higher values because the MEMS beam enters the

buckling regime [29]. When  $x_0/h > 0$ , the frequency levels off instead of dropping to zero, and the steep frequency change also gradually disappears as  $x_0$  increases, which is not conducive to achieving high sensitivity [15]. Please note that, as  $x_0$  increases, the lowest resonance frequency that can be achieved by strain tuning increases, and the buckling point shifts to a lower strain ( $\varepsilon/\varepsilon_{cr} < 1$ ), as indicated by the marks in Fig. 1(d). Here, we define the point where the frequency polarity changes in each curve as the buckling point (buckling condition), and its corresponding strain is called buckling strain. As shown in Fig. 1(d), the buckling strains for  $x_0/h = 0-0.20$  are  $\varepsilon/\varepsilon_{cr} = 1, 0.85, 0.72, 0.65$ , and  $0.59$ .

From Eq. (11), we know that the cubic nonlinearity coefficient,  $\alpha$ , is not affected by the compressive strain, but the quadratic nonlinearity coefficient,  $\beta$ , is proportional to  $x_T$ . We therefore plot the calculated  $\beta$  as a function of  $\varepsilon/\varepsilon_c$  on the right  $y$  axis of Fig. 1(b). As seen, for the cases of  $x_0 > 0$ ,  $\beta$  generally increases with increased compressive strain, and the increase in  $\beta$  becomes steeper when the value of  $\varepsilon/\varepsilon_{cr}$  approaches the buckling strain. Since  $\beta$  gives a softening nonlinearity, such a steep increase in quadratic (softening) nonlinearity is expected to dramatically compensate for cubic (hardening) nonlinearity, resulting in modulating total nonlinearity significantly.

To show the strain-tuning effect on the suppression of frequency shift, here, we take the case of the initial center deflection of  $x_0/h = 0.1$  as an example. Regarding other cases of initial center deflection, please see the Supplemental Material [30]. Figure 2 plots the normalized resonance frequency,  $f/f_0$ , as a function of the oscillation amplitude, as calculated for various  $\varepsilon/\varepsilon_{cr}$  in the case of  $x_0/h = 0.1$ . As seen, when the compressive strain is small, the resonance-frequency shift to the higher-frequency side with increasing oscillation amplitude, and

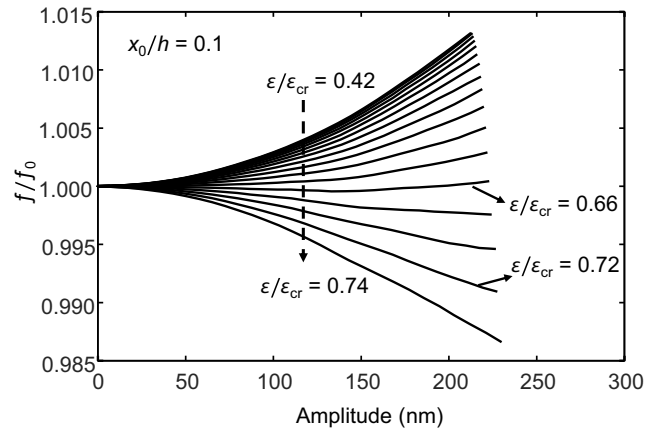


FIG. 2. Calculated resonance frequency ( $f/f_0$ ) as a function of oscillation amplitude at various  $\varepsilon/\varepsilon_{cr}$  values; initial center deflection is  $x_0/h = 0.1$ . Frequency is normalized by the natural frequency,  $f_0$ , without oscillation.

the nonlinearity does not change significantly, indicating that the hardening cubic nonlinearity dominates the total nonlinearity. However, as compressive strain approaches buckling strain ( $\varepsilon/\varepsilon_{\text{cr}}=0.72$ ), the positive frequency shift is significantly reduced, owing to the enhanced quadratic softening nonlinearity, and the frequency shift reaches a minimum at  $\varepsilon/\varepsilon_{\text{cr}}=0.66$ . When the compressive strain exceeds  $\varepsilon/\varepsilon_{\text{cr}}=0.66$ , the resonance-frequency shift to the lower-frequency side, indicating that the total nonlinearity is tuned to softening under this condition. We therefore conclude that the nonlinearity of the MEMS beam can be well suppressed by approaching the buckling condition of the MEMS beam.

In addition, we also find that, although nonlinearity can be controlled by increasing  $x_0$  without applying compressive strain, a large  $x_0$  will reduce the responsivity of the MEMS resonator (see the Supplemental Material for more details [30]), which is not preferable for high-sensitivity sensing applications [15]. Thus, in this work, we try to suppress  $x_0$  to a very small value ( $x_0/h \sim 0.01$ ) to achieve both a large responsivity and a small nonlinearity by approaching the buckling condition.

#### IV. EXPERIMENTAL SETUP AND RESULTS

The electrothermal effect [20] and lattice mismatch [21] are proposed to induce strain in MEMS beam resonators. Since the electrothermal effect may induce some additional noise during heating, we demonstrate nonlinearity control of MEMS beam resonators using the compressive strain induced by lattice mismatch in this work. We grow an  $\text{In}_x\text{Ga}_{1-x}\text{As}/(\text{Al}, \text{Ga})\text{As}$  heterostructure on a GaAs substrate, the structure of which is schematically shown in Fig. 3(a). Owing to the lattice mismatch between InAs and GaAs, there is compressive strain preloaded into the  $\text{In}_x\text{Ga}_{1-x}\text{As}$  layer, as given by [21]

$$\varepsilon_l = \left( \frac{a_{\text{InAs}}}{a_{\text{GaAs}}} - 1 \right) x, \quad (14)$$

where  $\alpha_{\text{InAs}}$  and  $\alpha_{\text{GaAs}}$  are the lattice constants of InAs and GaAs, respectively, and  $x$  represents the content of indium in  $\text{In}_x\text{Ga}_{1-x}\text{As}$ . After growing a 100-nm-thick GaAs buffer layer and a 2- $\mu\text{m}$ -thick  $\text{Al}_{0.7}\text{Ga}_{0.3}\text{As}$  sacrificial layer on a GaAs substrate, the beam layer is formed by depositing a GaAs/ $\text{Al}_{0.3}\text{Ga}_{0.7}\text{As}$  superlattice buffer layer and a 1- $\mu\text{m}$ -thick  $\text{In}_{0.004}\text{Ga}_{0.996}\text{As}$  layer. Here, the superlattice buffer layer is used to ensure the homogenous growth of the beam layer in the wafer growth by MBE [31]. Then, we form a two-dimensional electron-gas (2DEG) layer by growing an 80-nm-thick  $n^+\text{Al}_{0.3}\text{Ga}_{0.7}\text{As}$  layer and a 10-nm-thick undoped GaAs capping layer. Figure 3(b) shows the schematic structure of the fabricated doubly clamped MEMS beam. The suspended beam is formed by selectively etching the sacrificial layer with diluted hydrofluoric

acid (HF). The mesa layer and two top NiCr gates (12 nm) on both ends of the beam form two piezoelectric capacitors,  $C_1$  and  $C_2$ , together with the 2DEG layer. A microscope image of the MEMS resonators is shown in Fig. 3(c). We drive the beam into oscillation by applying an ac voltage ( $V_D$ ) to one of the piezoelectric capacitors and then measure the beam oscillation by a laser Doppler vibrometer and a lock-in amplifier with a built-in phase-locked loop (PLL). In addition, we deposit a 12-nm-thick NiCr layer on the middle part of the beam as a heater for calibrating the thermal response. All the measurements are performed under vacuum ( $\sim 10^{-4}$  Torr) at room temperature.

Since the nonlinearity is expected to be significantly modulated near the buckling point of the MEMS beam and the buckling point is close to  $\varepsilon/\varepsilon_{\text{cr}}=1$  for a small  $x_0$  [see Fig. 1(d)], the lattice-mismatch strain,  $\varepsilon_l$ , must be close to  $\varepsilon_{\text{cr}}$ . However, it is difficult to grow many  $\text{In}_x\text{Ga}_{1-x}\text{As}$  wafers with various indium concentrations. Since  $\varepsilon_{\text{cr}}$  is a function of beam length,  $L$  [ $\varepsilon_{\text{cr}} = (\pi^2/3)(h^2/L^2)$ ], in this work, we realize the buckling condition by varying the length of the MEMS beams to make  $\varepsilon_{\text{cr}}$  approach the fixed  $\varepsilon_l$ , and thus, modulate the nonlinearity. We fabricate  $\text{In}_{0.004}\text{Ga}_{0.996}\text{As}$  MEMS beam resonators with various beam lengths,  $L = 51\text{--}111 \mu\text{m}$ , and measure the resonance frequency with a driving voltage of  $V_D = 20$  mV. Figure 4(a) shows the resonance frequency (lines, theoretical calculation; dots, experimental results) of the  $\text{In}_{0.004}\text{Ga}_{0.996}\text{As}$  beams as a function of  $L$ . As seen, the measured resonance frequency reasonably agrees with that of theoretical calculations at  $x_0/h = 0.01$ , indicating that the initial center deflection is about 10 nm for the present MEMS beam resonators, which may come from plastic deformation during the fabrication process. Furthermore, the frequency polarity changes at  $L = 103 \mu\text{m}$ , which is regarded as the buckling point, and a small nonlinearity (i.e., small resonance-frequency shift) is expected to be observed near this point.

To estimate the mechanical nonlinearity of the MEMS beams and compare it with the theoretical calculation results, we drive the MEMS resonator at different amplitudes and measure the resonance frequencies ( $f$ ). The MEMS resonator is driven at a self-sustained oscillation mode at various driving voltages ( $V_D = 10\text{--}400$  mV) by using a PLL. Figure 4(b) plots the calculated resonance-frequency shift ( $\Delta f = f - f_0$ ) as a function of oscillation amplitude at various  $L$  (97–105  $\mu\text{m}$ ). As seen in Fig. 4(b), for a small oscillation amplitude ( $\sim 100$  nm), with the beam length varying from 97 to 105  $\mu\text{m}$ ,  $\Delta f$  is first reduced and reaches a minimum at  $L = 101 \mu\text{m}$ , and then shifts to the negative side, indicating that the nonlinearity is tuned from hardening to softening. However, at the large oscillation-amplitude range ( $\gtrsim 200$  nm), the resonance frequencies of  $L > 101 \mu\text{m}$  shift to higher frequency again. This result indicates that the nonlinearity at small amplitudes is softening but hardening at large amplitudes, which can be

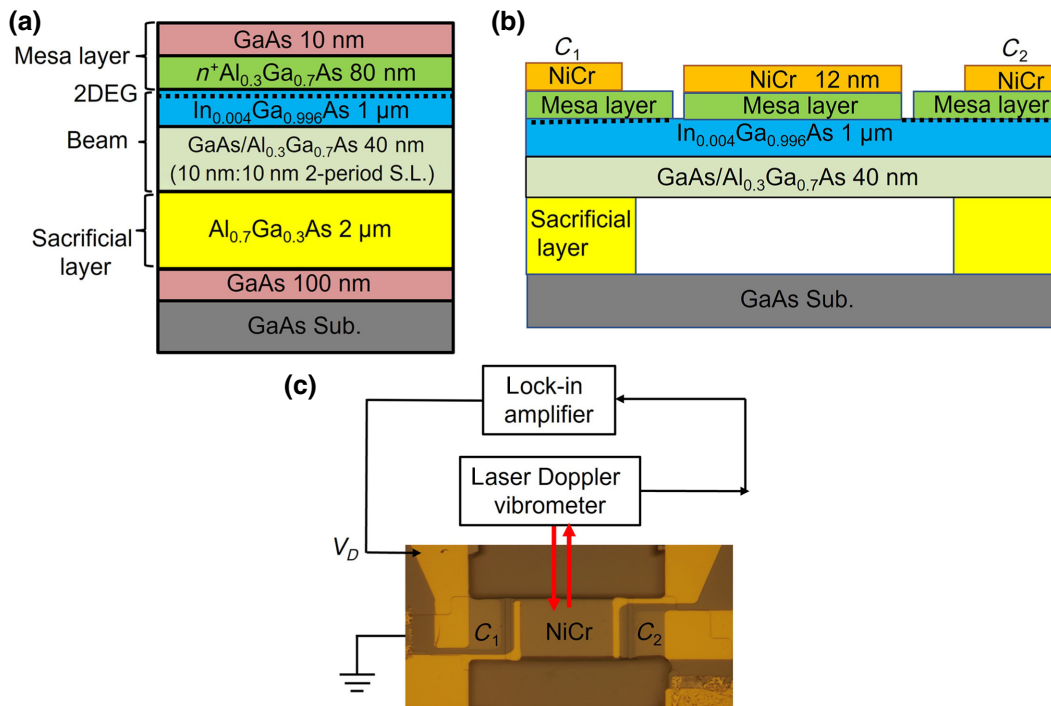


FIG. 3. (a) Wafer structure used for fabricating the In<sub>0.004</sub>Ga<sub>0.996</sub>As MEMS beam resonators. (b) Schematic structure of the fabricated doubly clamped MEMS beam. Mesa layer and two top gates (NiCr = 12 nm) on both ends of the beam form two piezoelectric capacitors, C<sub>1</sub> and C<sub>2</sub>, together with the 2DEG layer. 12-nm-thick NiCr layer is deposited as a heater for calibrating the thermal response. (c) Microscope image of the fabricated MEMS beam resonator. An ac voltage is applied to one of the piezoelectric capacitors to drive the resonator, and the induced mechanical oscillation is measured by a laser Doppler vibrometer and a lock-in amplifier with a built-in PLL.

understood by the fact that the hardening nonlinearity is cubic, but the softening nonlinearity is quadratic. Since the orders of the two nonlinearities are different, the total nonlinearity depends on the oscillation amplitude.

Figure 4(c) shows the measured resonance-frequency shift ( $\Delta f$ ) of In<sub>0.004</sub>Ga<sub>0.996</sub>As samples as a function of the oscillation amplitude with various  $L$ . As seen,  $\Delta f$  changes from positive to negative as the beam length increases, indicating the nonlinearity is tuned from hardening to softening. For a small oscillation-amplitude range (0–100 nm),  $\Delta f$  reaches a minimum at  $L = 101 \mu\text{m}$ , which is consistent with the theoretical calculations in Fig. 4(b). Moreover,  $\Delta f$  does not change significantly from  $L = 51 \mu\text{m}$  to  $L = 97 \mu\text{m}$  but is rapidly tuned near the buckling point. This is because the increase in the quadratic nonlinearity coefficient,  $\beta$ , becomes steeper near the buckling condition. The above results demonstrate that the MEMS resonator exhibits a small nonlinearity by approaching the buckling condition of the MEMS beam.

It is found that the calculated  $\Delta f$  agrees with experimental data nicely for small- and moderate-amplitude ranges (0–200 nm). However, at larger amplitudes (>200 nm), there is a notable discrepancy between calculated  $\Delta f$  [Fig. 4(b)] and measurement data [Fig. 4(c)]. Such a discrepancy may be owing to the fluctuation of

the beam lengths ( $L$ ). In Fig. 4(c), the beam length,  $L$ , is a designed value. The actual beam length, however, may be slightly shorter or longer owing to random fabrication errors, which give different experimental  $\Delta f$  from the calculation results. Furthermore, the theoretical model shown in this research is based on an approximation of the cubic nonlinearity of the MEMS beam [see Eq. (4) in Ref. [23]]. However, the higher-order nonlinearities (e.g., 5th, 7th. . .) also exist and may contribute to discrepancies between experiments and calculations at very large oscillation amplitudes. Nevertheless, the trend of the nonlinearity changes with beam length is well shown in both numerical and experimental results.

At a large oscillation amplitude, the polarity change of  $\Delta f$  predicted by the numerical result is observed. Figure 4(d) plots a magnification of the measured  $\Delta f$ -amplitude curve for the MEMS beam with  $L = 103 \mu\text{m}$ , together with the numerical  $\Delta f$ -amplitude curve for  $L = 104 \mu\text{m}$ , where the resonance frequency first decreases at small amplitudes but levels off and then increases at large amplitudes, as indicated by the red arrows. As seen, the experimental result for  $L = 103 \mu\text{m}$  shows good agreement with the numerical result for  $L = 104 \mu\text{m}$ , indicating that the actual beam length of this sample is probably closer to 104  $\mu\text{m}$  rather than the designed 103  $\mu\text{m}$ . It should

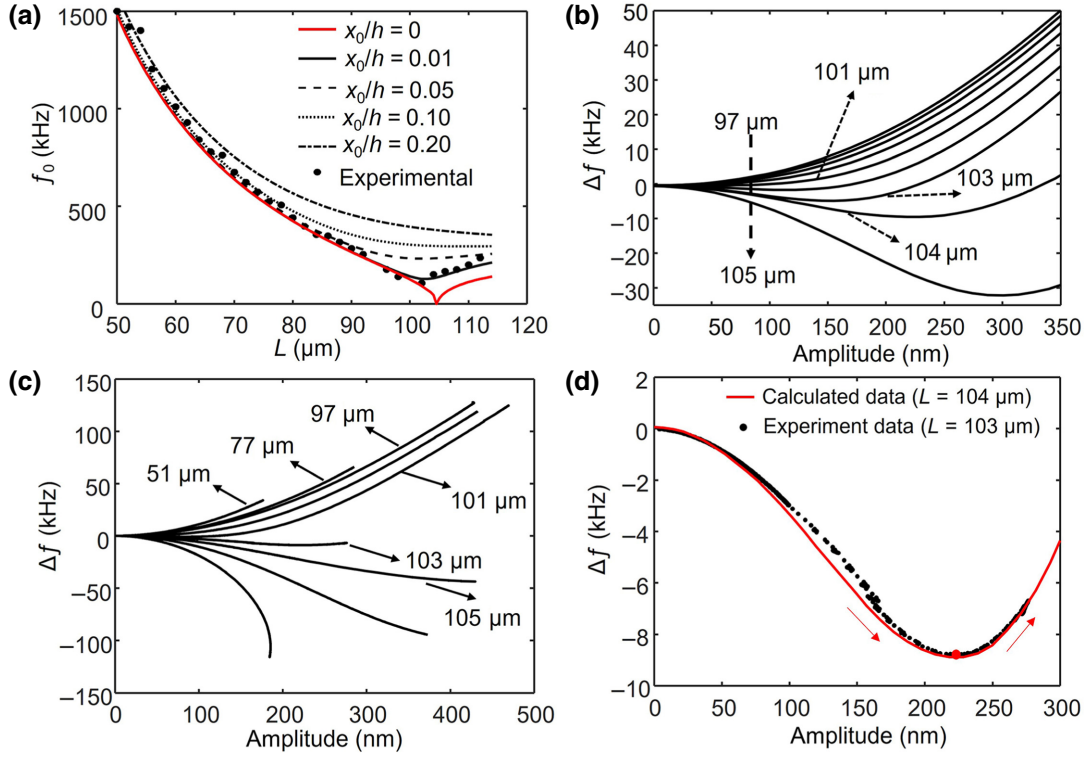


FIG. 4. (a) Resonance frequency (lines, theoretical calculations; dots, experimental results) of the  $\text{In}_{0.004}\text{Ga}_{0.996}\text{As}$  beams as a function of  $L$ . (b) Calculated resonance-frequency shifts ( $\Delta f$ ) as a function of oscillation amplitude at various  $L$  (97–105  $\mu\text{m}$ ). (c) Measured resonance-frequency shifts ( $\Delta f$ ) of  $\text{In}_{0.004}\text{Ga}_{0.996}\text{As}$  samples with various  $L$ . (d) Magnification of the measured  $\Delta f$ -amplitude curve for the MEMS beam with  $L = 103 \mu\text{m}$  (dots), together with the numerical  $\Delta f$ - $a$  curves for  $L = 104 \mu\text{m}$  (line). Red arrows show the change in resonant frequency. At the zero-dispersion point (red dot), there is an extremum of frequency with zero slope, and hence, frequency is locally independent of amplitude.

be noted that the boundary condition where the nonlinearity changes polarity [shown by the red dot in Fig. 4(d)] is given a zero-dispersion point [32,33], where the resonance frequency is locally independent of the amplitude ( $d\omega/dE=0$ ). Thus, at this point, the amplitude fluctuation does not induce additional frequency noise, which is similar to the linear oscillation regime, but its oscillation amplitude is much larger than the linear oscillation amplitude without the preloaded lattice-mismatch strain. Therefore, the zero-dispersion point is very promising for low-noise sensing applications.

To intuitively show the effects of  $\alpha$  and  $\beta$  on the total nonlinearity ( $Y_T$ ) of the MEMS beam, we estimate  $Y_T$  by fitting the equation described in Ref. [34]:

$$f = f_0(1 + Y_T A^2), \quad (15)$$

where  $f$  and  $f_0$  are the measured resonance frequency and the natural resonance frequency without oscillation, respectively, and  $A$  is the oscillation amplitude. The fitting is performed over a small oscillation-amplitude range of approximately 0–50 nm, with data shown in Fig. 4(c). The results are shown by dots in Fig. 5(a). As seen,  $Y_T$  keeps a stable value when the beam length is small ( $L \lesssim 100 \mu\text{m}$ ),

and quickly drops to a negative value when approaching the buckling condition ( $L = 103 \mu\text{m}$ ). When  $L$  exceeds about 108  $\mu\text{m}$ ,  $Y_T$  rises from the negative value ( $|Y_T|$  decreases).

To understand the origin of the nonlinearity change, we calculate the effective nonlinearity,  $Y_{(\alpha,\beta)}$ , by using the cubic ( $\alpha$ ) and quadratic ( $\beta$ ) nonlinearity coefficients and, following the equation described in Ref. [35]:

$$Y_{(\alpha,\beta)} = \frac{3}{8} \frac{\alpha}{\omega_0^2} - \frac{5}{12} \frac{\beta^2}{\omega_0^4}, \quad (16)$$

where  $\omega_0 = 2\pi f_0$ . In addition, to quantitatively understand how  $\alpha$  and  $\beta$  affect the effective nonlinearity, we also calculate  $Y_{(\alpha)} = (3/8)(\alpha/\omega_0^2)$  and  $Y_{(\beta)} = -(5/12)(\beta^2/\omega_0^4)$ . The calculated  $Y_{(\alpha,\beta)}$ ,  $Y_{(\alpha)}$ , and  $Y_{(\beta)}$  are shown by the black, blue, and red curves, respectively, in Fig. 5(a). The values of  $\alpha$  and  $\beta$  used for this calculation are shown as the solid and dashed curves in Fig. 5(b). As seen in Fig. 5(a), calculated  $Y_{(\alpha,\beta)}$  reasonably agrees with experimental  $Y_T$ . When  $L$  is small ( $L < 100 \mu\text{m}$ ),  $Y_{(\alpha,\beta)}$  and  $Y_{(\alpha)}$  have the same traces, indicating the nonlinearity is dominated by the  $\alpha$  term under this condition. The MEMS beam thus exhibits hardening nonlinearity. Furthermore,

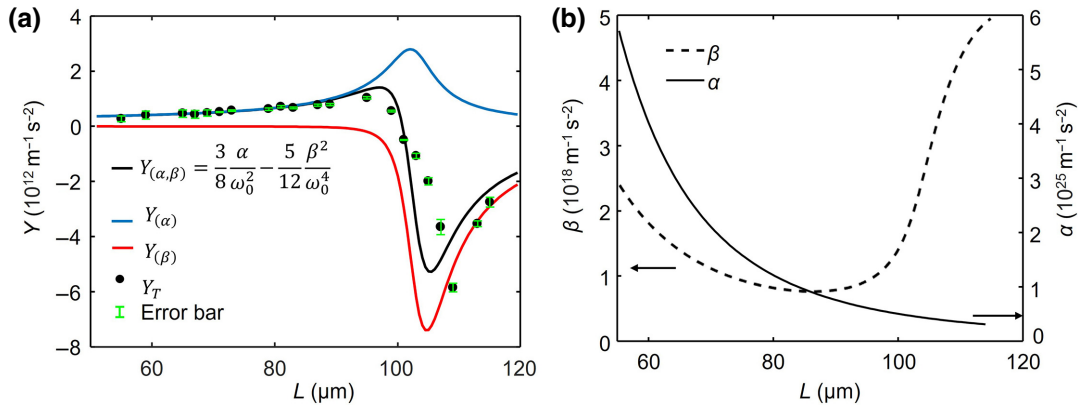


FIG. 5. (a) Estimated total nonlinearity,  $Y_T$ , and calculated effective nonlinearity coefficient,  $Y_{(\alpha,\beta)}$ , as well as its two terms,  $Y_{(\alpha)}$  and  $Y_{(\beta)}$ , as a function of  $L$ .  $Y_T$  is estimated by linear fitting, using data at an oscillation-amplitude range of approximately 0–50 nm in Fig. 4(c). (b) Calculated cubic nonlinearity coefficient,  $\alpha$ , and quadratic nonlinearity coefficient,  $\beta$ , as a function of  $L$ .

we can see that  $Y_{(\alpha)}$  does not change much with increasing  $L$  before reaching the buckling condition. This is because, although  $\alpha$  decreases with  $L$ , as shown in Fig. 5(b),  $\omega_0$  also decreases with  $L$  [see Fig. 4(a)], giving a stable  $Y_{(\alpha)}$  and, furthermore, a stable  $Y_{(\alpha,\beta)}$  ( $\beta$  is very small in this case). However,  $Y_{(\alpha,\beta)}$  changes its trend to be the same as  $Y_{(\beta)}$  when approaching the buckling condition, indicating the nonlinearity is dominated by the  $\beta$  term from this point. As a result,  $Y_{(\alpha,\beta)}$  quickly drops to a negative value, owing to the large increase in  $\beta$  [see Fig. 5(b)]; a quasizero nonlinearity is thereby achieved near the buckling condition. Moreover, there is a reversal of polarity in  $Y_{(\alpha,\beta)}$  when  $L$  exceeds about 105  $\mu\text{m}$ , which is because  $\omega_0$  starts to increase with the further increase in  $L$  [(see Fig. 4(a)).

Note that there is a small difference in the lengths where  $Y_T$  and  $Y_{(\alpha,\beta)}$  achieve the minimum value. This is probably because the experimental beam lengths may be slightly different from the designed values, or the control of indium composition is not perfect ( $x$  in  $\text{In}_x\text{Ga}_{1-x}\text{As}$ ) during wafer growth, and the buckling condition is very sensitive to the beam length and actual  $x$ . However, the main feature of the experimental nonlinearity ( $Y_T$ ) is well reproduced by the numerically calculated nonlinearity ( $Y_{(\alpha,\beta)}$ ).

## V. CONCLUSION

We clarify the mechanism of the strain-tuning effect on mechanical nonlinearity in doubly clamped GaAs MEMS beam resonators and demonstrate that mechanical nonlinearity can be greatly suppressed by preloading a lattice-mismatch strain in the MEMS beam. The nonlinearity of the MEMS beam arises from the hardening- and softening-nonlinearity terms in the Duffing equation. By approaching the buckling condition of the MEMS beam, the softening nonlinearity greatly compensates for the hardening nonlinearity, and the total nonlinearity is thus suppressed. Utilizing this knowledge, we fabricate  $\text{In}_x\text{Ga}_{1-x}\text{As}$  MEMS

beams working near the buckling condition and measure the frequency shift as a function of oscillation amplitude. As a result, the frequency shift of the MEMS resonator is well suppressed near the buckling condition, and a zero-dispersion operation point is achieved, which is very promising for low-noise sensing applications with MEMS resonators. The demonstrated approach provides a promising path to suppress the nonlinearity of the MEMS beam and enables the low-noise operation of MEMS resonators. Furthermore, the use of effective nonlinearity to reproduce total nonlinearity intuitively shows the effect of hardening and softening nonlinearities on the total nonlinearity, allowing one to understand the origin of the nonlinearity change.

## ACKNOWLEDGMENTS

This work is partly supported by the A-STEP program of JST, a MEXT Grant-in-Aid for Scientific Research on Innovative Areas “Science of hybrid quantum systems” (Grant No. 15H05868), and a KAKENHI grant from JSPS (Grant No. 21K04151).

- [1] K. Ekinici and M. Roukes, Nanoelectromechanical systems, *Rev. Sci. Instrum.* **76**, 061101 (2005).
- [2] A. Boisen, S. Dohn, S. S. Keller, S. Schmid, and M. Tenje, Cantilever-like micromechanical sensors, *Rep. Prog. Phys.* **74**, 036101 (2011).
- [3] A. N. Cleland, *Foundations of Nanomechanics: From Solid-State Theory to Device Applications* (Springer, New York, 2003).
- [4] K. L. Ekinici, X. M. H. Huang, and M. L. Roukes, Ultrasensitive nanoelectromechanical mass detection, *Appl. Phys. Lett.* **84**, 4469 (2004).
- [5] S. Dohn, R. Sandberg, W. Svendsen, and A. Boisen, Enhanced functionality of cantilever based mass sensors using higher modes, *Appl. Phys. Lett.* **86**, 233501 (2005).



- [6] K. Jensen, K. Kim, and A. Zettl, An atomic-resolution nanomechanical mass sensor, *Nat. Nanotechnol.* **3**, 533 (2008).
- [7] D. Rugar, R. Budakian, H. Mamin, and B. Chui, Single spin detection by magnetic resonance force microscopy, *Nature* **430**, 329 (2004).
- [8] A. N. Cleland and M. L. Roukes, A nanometre-scale mechanical electrometer, *Nature* **392**, 160 (1998).
- [9] R. Knobel, C. S. Yung, and A. N. Cleland, Single-electron transistor as a radio-frequency mixer, *Appl. Phys. Lett.* **81**, 532 (2002).
- [10] X. Wang, X. Wei, D. Pu, and R. Huan, Single-electron detection utilizing coupled nonlinear microresonators, *Microsyst. Nanoeng.* **6**, 78 (2020).
- [11] A. K. Pandey, O. Gottlieb, O. Shtempluck, and E. Buks, Performance of an AuPd micromechanical resonator as a temperature sensor, *Appl. Phys. Lett.* **96**, 203105 (2010).
- [12] T. Larsen, S. Schmid, L. Grönberg, A. Niskanen, J. Hassel, S. Dohn, and A. Boisen, Ultrasensitive string-based temperature sensors, *Appl. Phys. Lett.* **98**, 121901 (2011).
- [13] A. Svetlitzka, T. Blank, S. Stolyarova, I. Brouk, S. B. L. Shefi, and Y. Nemirovsky, CMOS-SOI-MEMS thermal antenna and sensor for uncooled THz imaging, *IEEE Trans. Electron Devices* **63**, 1260 (2016).
- [14] X. C. Zhang, E. B. Myers, J. E. Sader, and M. L. Roukes, Nanomechanical torsional resonators for frequency-shift infrared thermal sensing, *Nano Lett.* **13**, 1528 (2013).
- [15] Y. Zhang, Y. Watanabe, S. Hosono, N. Nagai, and K. Hirakawa, Room temperature, very sensitive thermometer using a doubly clamped microelectromechanical beam resonator for bolometer applications, *Appl. Phys. Lett.* **108**, 163503 (2016).
- [16] Y. Zhang, S. Hosono, N. Nagai, S.-H. Song, and K. Hirakawa, Fast and sensitive bolometric terahertz detection at room temperature through thermomechanical transduction, *J. Appl. Phys.* **125**, 151602 (2019).
- [17] T. Fukuma, M. Kimura, K. Kobayashi, K. Matsushige, and H. Yamada, Development of low noise cantilever deflection sensor for multienvironment frequency-modulation atomic force microscopy, *Rev. Sci. Instrum.* **76**, 053704 (2005).
- [18] D. Antonio, D. H. Zanette, and D. López, Frequency stabilization in nonlinear micromechanical oscillators, *Nat. Commun.* **3**, 806 (2012).
- [19] Y. Zhang, Y. Yoshioka, I. Morohashi, and X. Liu, 1:1 internal mode coupling strength in GaAs doubly-clamped MEMS beam resonators with linear and nonlinear oscillations, *Appl. Phys. Express* **14**, 014001 (2021).
- [20] Y. Zhang, Y. Yoshioka, M. Iimori, B. Qiu, X. Liu, and K. Hirakawa, Thermal tuning of mechanical nonlinearity in GaAs doubly-clamped MEMS beam resonators, *Appl. Phys. Lett.* **119**, 163503 (2021).
- [21] B. Qiu, Y. Zhang, N. Nagai, and K. Hirakawa, Enhancing the thermal responsivity of microelectromechanical system beam resonators by preloading a critical buckling strain, *Appl. Phys. Lett.* **119**, 153502 (2021).
- [22] Mohammad I. Younis, *MEMS Linear and Nonlinear Statics and Dynamics* (Springer, New York, 2011).
- [23] Ron Lifshitz, and Michael C. Cross, Nonlinear dynamics of nanomechanical and micromechanical resonators (Reviews of nonlinear dynamics and complexity 1.1, 2008).
- [24] F. Tajaddodianfar, M. R. H. Yazdi, and H. N. Pishkenari, Nonlinear dynamics of MEMS/NEMS resonators: analytical solution by the homotopy analysis method, *Microsyst. Technol.* **23**, 1913 (2017).
- [25] A. Z. Hajjaj, M. A. Hafiz, and M. I. Younis, Mode coupling and nonlinear resonances of MEMS arch resonators for bandpass filters, *Sci. Rep.* **7**, 41820 (2017).
- [26] F. Tajaddodianfar, M. R. H. Yazdi, H. N. Pishkenari, and E. M. Miandoab, in *2014 IEEE/ASME International Conference on Advanced Intelligent Mechatronics (IEEE)*, pp. 1284–1289.
- [27] S. Neumeyer, V. S. Sorokin, and J. J. Thomsen, Effects of quadratic and cubic nonlinearities on a perfectly tuned parametric amplifier, *J. Sound Vib.* **386**, 327 (2017).
- [28] S. A. Tella, A. Z. Hajjaj, and M. I. Younis, The effects of initial rise and axial loads on MEMS arches, *J. Vib. Acoust.* **139**, 040905 (2017).
- [29] A. Z. Hajjaj, N. Alcheikh, A. Ramini, M. A. Al Hafiz, and M. I. Younis, Highly tunable electrothermally and electrostatically actuated resonators, *J. Microelectromech. Syst.* **25**, 440 (2016).
- [30] See the Supplemental Material at <http://link.aps.org/supplemental/10.1103/PhysRevApplied.19.024025> for more details about the effect of the initial center deflection and compressive strain on nonlinearity and responsivity.
- [31] I. Mahboob and H. Yamaguchi, Bit storage and bit flip operations in an electromechanical oscillator, *Nat. Nanotechnol.* **3**, 275 (2008).
- [32] S. Rosenberg and O. Shoshani, Zero-dispersion point in curved micro-mechanical beams, *Nonlinear Dyn.* **107**, 1 (2021).
- [33] L. Huang, S. Soskin, I. Khovanov, R. Mannella, K. Ninios, and H. B. Chan, Frequency stabilization and noise-induced spectral narrowing in resonators with zero dispersion, *Nat. Commun.* **10**, 3930 (2019).
- [34] L. L. Li, P. M. Polunin, S. Dou, O. Shoshani, B. S. Strachan, J. S. Jensen, S. W. Shaw, and K. L. Turner, Tailoring the nonlinear response of MEMS resonators using shape optimization, *Appl. Phys. Lett.* **110**, 081902 (2017).
- [35] S. Dou, B. S. Strachan, S. W. Shaw, and J. S. Jensen, Structural optimization for nonlinear dynamic response, *Philos. Trans. R. Soc., A* **373**, (2015).